

X-ray imaging in advanced studies of ophthalmic diseases

Andrea Antunes

Instituto de Física, Universidade de São Paulo, São Paulo, SP, Brazil

Angélica M. V. Safatle and Paulo S. M. Barros

Faculdade de Medicina Veterinária, Universidade de São Paulo, São Paulo, SP, Brazil

Sérgio L. Morelhão^{a)}

Instituto de Física, Universidade de São Paulo, CP 66318, 05315-970, São Paulo, SP, Brazil

(Received 17 December 2005; revised 27 March 2006; accepted for publication 27 April 2006; published 19 June 2006)

Microscopic characterization of pathological tissues has one major intrinsic limitation, the small sampling areas with respect to the extension of the tissues. Mapping possible changes on vast tissues and correlating them with large ensembles of clinical cases is not a feasible procedure for studying most diseases, as for instance vision loss related diseases and, in particular, the cataract. Although intraocular lens implants are successful treatments, cataract still is a leading public-health issue that grows in importance as the population increases and life expectancy is extended worldwide. In this work we have exploited the radiation-tissue interaction properties of hard x-rays—very low absorption and scattering—to map distinct lesions on entire eye lenses. At the used synchrotron x-ray photon energy of 20 keV (wavelength $\lambda=0.062$ nm), scattering and refraction are angular resolved effects. It allows the employed x-ray image technique to efficiently characterize two types of lesions in eye lenses under cataractogenesis: distributions of tiny scattering centers and extended areas of fiber cell compaction. The data collection procedure is relatively fast; allowing dozens of samples to be totally imaged (scattering, refraction, and mass absorption images) in a single day of synchrotron beam time. More than 60 cases of canine cataract, not correlated to specific causes, were investigated in this first application of x-rays to image entire lenses. Cortical opacity cases, or partial opacity, could be related to the presence of calcificated tissues at the cortical areas, clearly visible in the images, whose elemental contents were verified by micro x-ray fluorescence as very rich in calcium. Calcificated tissues were also observed at nuclear areas in some cases of hypermature cataract. Total opacity cases without distinguishable amount of scattering centers consist in 70% of the analyzed cases, where remarkable fissure marks owing to extended areas of fiber cell compaction are diagnosed. © 2006 American Association of Physicists in Medicine. [DOI: 10.1118/1.2207135]

Key words: crystalline lens, x-ray imaging, x-ray radiography, cataract, synchrotron radiation

I. INTRODUCTION

Vision systems of mammals are susceptible to a variety of diseases related to alterations in the optical/physiological properties of the tissues responsible for processing the visible light inside the eye. Understanding the causes at molecular level is necessary for prevention or correction of vision loss at early stages of the diseases. This fact has motivated much research during the last decades.^{1–13} Visible light and electron beams are among the most used probes in such research, but they have inherent limitations regarding either high amount of scattering (light) or shallow penetration depth (electrons). To minimize light scattering, in order to improve resolution, histological procedures (thin samples) are required for optical microscopy, and similar procedures are necessary in electron microscopy since the probing depth is very small. Consequently, light and electron beam methods are not feasible for providing information of reasonable resolution on macroscopic scales.

Here we report advantages in using x-rays to obtain images of good resolution (tens of microns) on extended tissues

(centimeter scales). It is possible, in principle, since at x-ray frequencies the scattering is restricted to very small angles and the penetration depth is incomparably larger than for electron beams. The necessary sensitivity to identify alteration in the tissues is achieved by employing an imaging technique where distinct radiation-tissue interaction processes are discriminated by Bragg diffraction into a highly perfect crystal prior to the image acquisition.^{14,15} The potential of x-ray imaging in ophthalmology is demonstrated by studying one of the most important eye diseases, the cataract.

Transparency loss of the eye lens, or cataract, occurs mostly due to visible light scattering. Although the biochemical and cellular changes leading to cataract are not well known,^{6,7,12,16,17} these changes have to induce density variations, or refraction index fluctuations, in a length scale D comparable to the wavelength λ in order to explain the visible light scattering that clouds the lenses. Since the angular spreading of the scattered light is roughly proportional to λ/D , shorter wavelength tools than light microscopy are required for probing the intrinsic nature of the scattering centers. Scanning electron microscopy has therefore been used

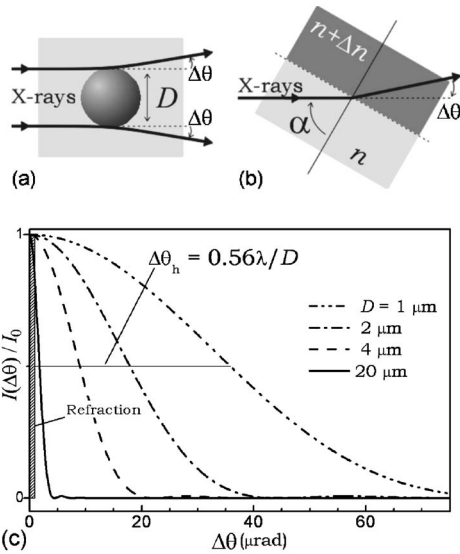


FIG. 1. Scattering (a) and refraction (b) of x-rays. Localized density variations in the tissue act as centers of scattering whose angular spreading of intensity $I(\Delta\theta)$, can be estimated by the theory of small-angle x-ray scattering (Ref. 18). (c) $I(\Delta\theta)$ calculated for spherical centers of several diameters D and $\lambda=0.062$ nm, Eqs. (1) and (2). Internal fluctuations $\Delta n/n$ of the refraction index in the tissue can deflect x-rays by nearly $1 \mu\text{rad}$, as given in Eq. (5), which is in general much smaller than the scattering by particles with $D < 20 \mu\text{m}$.

in searching for potential scattering centers.^{2,6} Fiber cell compactness—observed in age-related nuclear cataract^{7,12}—can generate density variations inside the lenses, but mapping the extension of compaction areas is necessary before relating fiber compaction to the light scattering observed in the cataractogenesis.

II. X-RAYS: SMALL-ANGLE SCATTERING AND REFRACTION

At short x-ray wavelengths, $\lambda < 0.1$ nm, the angular spreading of scattering is very small regarding visible light scattering but significantly above a few microradians for scattering centers with cross section below tens of microns. For instance, by assuming spherical scattering centers of uniform density with diameter D , the range of the angular spreading can be calculated from the x-ray small-angle scattering theory¹⁸ where

$$I(u) = I_0 |3(\sin u - u \cos u)/u^3|^2 \tag{1}$$

stands for the intensity distribution around the incident beam of intensity I_0 ,

$$u = \frac{2\pi}{\lambda} D \sin\left(\frac{\Delta\theta}{2}\right), \tag{2}$$

and $\Delta\theta$ is the deviation from the incident beam direction as defined in Fig. 1(a). At the half intensity $I(u)/I_0=1/2$, the deviation is

$$\Delta\theta_h \approx 0.56 \frac{\lambda}{D}. \tag{3}$$

For $\lambda=0.1$ nm and $D < 20 \mu\text{m}$, the angular spreading is estimated as being $\Delta\theta_h > 2.8 \mu\text{rad}$.

Refraction through fiber cells can produce slight angular deviations of the order of $1 \mu\text{rad}$ for density fluctuations as small as 10%. At the x-ray frequencies, the real part of the refraction index $n=1-\delta$, differs from unit by the very small number

$$\delta = 2.7 \times 10^{-4} \left(\frac{Z}{M}\right) \lambda^2 \rho, \tag{4}$$

where Z and M are the effective atomic number of the molecule and the molecular weight, respectively. λ is given in nanometers and the density of the tissue ρ , in g/cm^3 . In most cases $Z/M \approx 0.5$, and typical values of δ are in the range from 10^{-6} to 10^{-5} . Soft tissues in general have $\rho \approx 1 \text{ g}/\text{cm}^3$, and $\delta = 1.5 \times 10^{-6}$ when taking $Z/M=10/18$ as for water.

Density fluctuation $\Delta\rho$, does lead to a relative variation $\Delta n/n = -\Delta\delta$ in the index of refraction, and consequently to a deviation

$$\Delta\theta \approx \Delta\delta \tan \alpha \approx 1.5 \times 10^{-6} \left(\frac{\Delta\rho}{\rho}\right) \tan \alpha \tag{5}$$

in the beam direction as shown in Fig. 1(b). This very small refraction effect is enhanced for values of α a close 90° , reaching values above $|\Delta\theta|=1 \mu\text{rad}$ even for $\Delta\rho/\rho = 0.1 (82^\circ < \alpha < 98^\circ)$.

Scattering and refraction are angular resolved effects, as compared in Fig. 1(c) for different values of D . Therefore, it is possible in principle to map both the distribution of scattering centers and the density fluctuations on entire lenses, i.e., probing areas and depths of centimeters since the mass absorption coefficient for hard x-ray (> 20 keV) is below $1 \text{ cm}^2/\text{g}$.¹⁹ However, it requires wide, uniform, and monochromatic beams of very low divergence as the basic conditions for the incident x-ray optics, and an image acquisition system capable to provide an angular resolution of about a few microradians.

III. MATERIALS AND METHODS

Synchrotron facilities, adapted for diffraction enhanced x-ray imaging, have incident and transmitted beam optics very suitable for probing inhomogeneities in the eye tissues. In a previous attempt,^{20,21} low photon flux at the desired wavelength range have allowed only slices (about 1 mm thick) of the lenses to be imaged. Cutting damages at surfaces and long exposure times do not collaborate for conclusive studies of ocular tissues by x-ray imaging. In the present work, carried out at the X15A station of the National Synchrotron Light Source (NSLS), Brookhaven National Laboratory, images of entire *in vitro* lenses were obtained with x-ray photons of 20 keV ($\lambda=0.062$ nm). As depicted in Fig. 2(a), the angular resolution of the detection system is provided by the width of the analyzer window, which is the acceptance angle for the 333 Bragg reflection in a highly

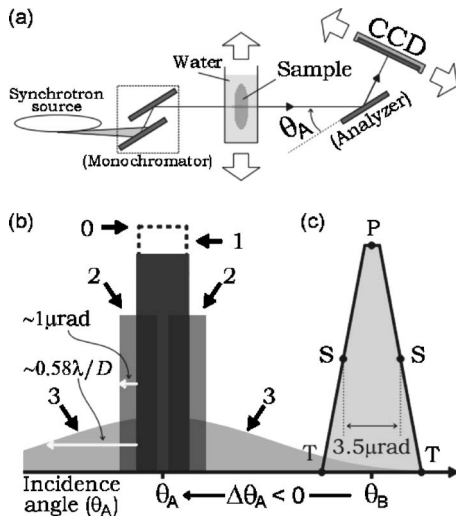


FIG. 2. (a) Experimental setup for synchrotron x-ray imaging of crystalline lenses. As the sample is scanned vertically through the horizontal fan of monochromatic x-ray beam, an array of CCD area detectors (pixel size of $50 \mu\text{m}$) is simultaneously scanned through the transmitted-diffracted beam (Ref. 15). (b) Transmitted beam. Interaction of the incident beam (arrow 0) with the tissue provides three major features on the transmitted beam: intensity reduction (arrow 1) due to absorption processes and/or scatterings; slight deviations (arrows 2) in the beam direction caused by refraction at the interface between large regions ($D > 20 \mu\text{m}$) of different densities; and scattering (arrows 3) due to surface roughness (in air exposures) or tiny regions of internal density fluctuations as for microscopic particles with ($D < 20 \mu\text{m}$). (c) Analyzer window provided by the acceptance angle θ_B for Bragg diffraction in a highly perfect analyzer crystal. Away from the analyzer tails, $|\Delta\theta_A| > 4 \mu\text{rad}$ (points T), only scattering is accepted in the CCDs. At the shoulders, $1 \mu\text{rad} < |\Delta\theta_A| < 2.5 \mu\text{rad}$ (points S), the diffracted intensities are very sensitive to the effect of refraction. Images collected with the analyzer window at $\Delta\theta_A = 0$ (point P) are mostly dominated by absorption contrast and pronounced reduction of intensity at the scattering centers.

perfect Si crystal, named analyzer crystal. At 20 keV, the full width at half-maximum of the analyzer's reflectivity curve is $3.5 \mu\text{rad}$ in the vertical plane. In practice it means that, when the analyzer is positioned at about 50% of reflectivity (shoulder of the analyzer window), the beam hitting the array of CCD detectors experiments intensity variations of more than 30% for just $1 \mu\text{rad}$ deviation from the incident beam direction. Since the intensity oscillation of the beam diffracted by the analyzer crystal is less than 5% at the NSLS,¹⁵ this set-up is sensitive even to deviations smaller than $1 \mu\text{rad}$. More details on the experimental setup are given in Fig. 2, as well as details on image formation criteria due to convolution of the transmitted beam, Fig. 2(b), with the analyzer window, Fig. 2(c).

All investigated cases of canine cataract were previously classified by ophthalmic exam as partial or total opacity regarding the extension of cloudiness in the lenses. All animals had severely compromised vision before surgery, but no correlation to specific causes was established. After capsular extraction all lenses, including some healthy ones, were maintained in fixative solution (formaldehyde 10%) for no longer than a few months. No perceptible alterations in color or opacity occurred during this period of time.

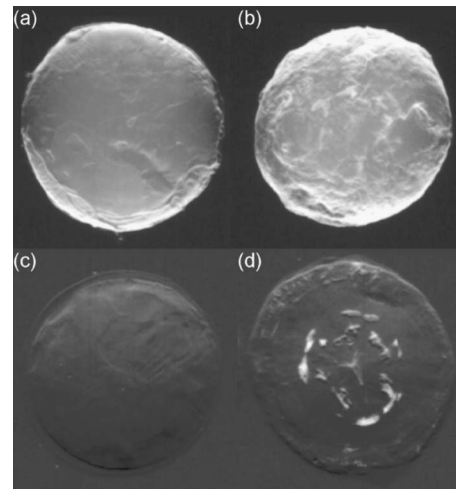


FIG. 3. X-ray refraction images of healthy and opaque crystalline lenses. Healthy (a) and opaque (b) lenses exposed in air. Healthy (c) and opaque (d) lenses exposed immersed in water. Exposures in air or water reveal mostly superficial or internal features, respectively. White areas in the opaque lens (d) are calcificated tissues, not distinguishable from surface scattering features when exposed in air (b). Analyzer crystal at $\Delta\theta_A = -1.2 \mu\text{rad}$. X-ray photon energy is 20 keV.

IV. RESULTS AND DISCUSSIONS

X-ray scattering owing to the air-tissue interface is very significant regarding most features inside the lenses. Images of lenses exposed in air, as in Figs. 3(a) and 3(b), can be useful to compare the surface morphology of healthy and cataractous lenses, but to reveal internal density fluctuations the majority of this surface scattering has to be avoided. It is possible by immersing the lenses in a medium of nearly the same density of the lens tissue, de-ionized water has been used for this purpose.²² A clean uniform low-contrast image is shown in Fig. 3(c) corresponding to the exposure of the healthy lens immersed in water. On the other hand, in-water exposure of the cataractous lens, shown in Fig. 3(d), reveals large high-density regions that were hindered by the surface scattering. Evidence of the higher density of these regions is the strong attenuation observed when recording the transmitted beam before the analyzer, as in conventional radiography, e.g., Fig. 4(b) where information on their internal location is also obtained.

Micro x-ray fluorescence ($100 \times 100 \mu\text{m}$ probe) carried out at the Brazilian Synchrotron Light Laboratory has confirmed that the white regions in Fig. 3(d) are very rich in calcium, and that most of the potassium present in the tissue is also located at these Ca-rich regions. Although both mineral elements were found at these regions, the fluorescence signal for potassium was less than 2% of that one for calcium. Calcificated tissues inside the lens—not only at its capsule—have been an unexpected finding, also checked by invasive procedures when cutting the sample for fluorescence analysis. The majority of the cases have shown calcificated tissues at the cortex close to the surface, e.g., Fig. 4(d). But, in advanced stages, as in the hypermature case shown here in Fig. 3(d), calcification could be found around nuclear areas. This fact indicates a migration of calcificated tissues

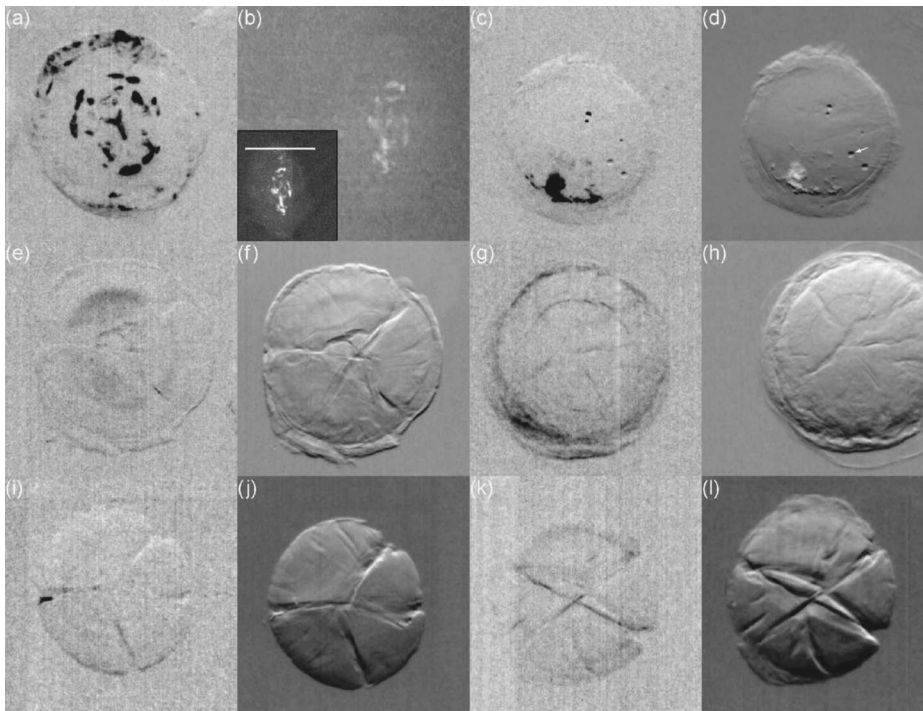


FIG. 4. Diffraction enhanced x-ray images of several cataractous lenses. (a), (c), (e), (g), (i), (k) Scattering images collected with the analyzer crystal positioned in the range $-5 \mu\text{rad} < \Delta\theta_A < -4 \mu\text{rad}$. (d), (f), (h), (j), (l) Refraction images with the analyzer crystal in the range $-2 \mu\text{rad} < \Delta\theta_A < -1 \mu\text{rad}$. The arrow in (d) indicates a small bubble air, showing opposite white/dark contrast than calcificated tissues. All exposures are for lenses immersed in water. (b) Lateral view of the calcificated lens in (a), exposed in air, and recorded on image plate before the analyzer crystal. The inset in (b) shows the mass density image (Ref. 22) composed from several images taken across the analyzer's rocking curve; bar stands for 1 cm, and the refraction image of this lens is shown in Fig. 3(d).

toward the nucleus during progression of the disease, which is in the same migration sense of the normal growth of the lenses from the outer epithelium to the inner nucleus.

In Fig. 4 the selectivity of the imaging technique for scattering and refraction effects is exploited for mapping separately both effects on several cases of cataract, some with different stages of calcification and others with no trace of calcification. Scattering images (S-images) were collected with the analyzer crystal at $\Delta\theta \approx -4.5 \mu\text{rad}$ from the center of its reflection curve ($<2\%$ of intensity, left tail), and refraction images (R-images) collected at $\Delta\theta \approx -1.5 \mu\text{rad}$ ($\sim 50\%$ of intensity, left shoulder). In the former type of image, the observed small-angle scattering around calcificated tissues, as in Figs. 4(a), 4(c), and 4(i) (small spot at left), corresponds to the expected one from compact aggregations of microscopic particles with $D < 8 \mu\text{m}$, Eq. (3). Such particles can be tiny calcium-rich deposits. Dilute distributions of microcalcifications could be responsible for the shading areas around the center of the image in Fig. 4(e), as well as for the dark borders in Fig. 4(g). R-images, as in Figs. 3(d), 4(d), and 4(j), have provided further evidence on the higher density of the aggregations regarding the surrounding healthy tissue. These images indicate that, at the core of the calcificated regions, the aggregates, or microcalcifications, have coalesced to form a continuous high-density tissue capable to refract the x-rays in opposite sense of an air bubble, as seen in Fig. 4(d).

Extended white/dark contrast marks running across the images, as in Figs. 4(f), 4(h), 4(j), and 4(l), is another type of feature to be investigated by x-ray imaging. Such marks are visible only under refraction sensitive conditions and they are nearly oriented at 120° from each other, which resemble the orientation of the anterior and posterior suture branches

found in most mammal lenses, commonly called Y sutures. Small amounts of scattering are sometimes observed along these refraction marks, as in the S-images in Figs. 4(e), 4(g), 4(i), and 4(k). The source of such scattering could be either accumulation of tiny aggregates along the marks or localized defects in the fiber cell organization in a length scale of a few microns, which is of the order of the width of the fibers ($\sim 7 \mu\text{m}$).¹³

Fiber cell compactness can explain the refraction marks. Simple arrangements of fiber cells, with density variation (compaction) along the length of the fibers, as illustrated in Fig. 5, could generate the observed white/dark contrast of the marks. However, in this type of arrangement no correlation to the threefold symmetry of the cortical fiber cell organiza-

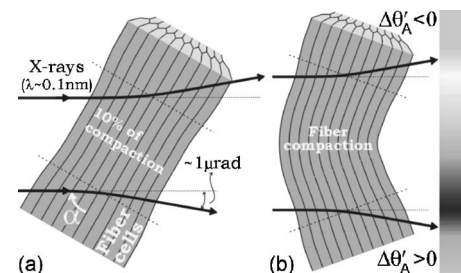


FIG. 5. Hypothetical arrangements of fiber cells: (a) linear and (b) bent arrays of fibers with compaction along their length producing white/dark contrast in refraction images. Fiber compactness can deflect x-rays according to Eq. (5) and, consequently, the component of this very small deflection—of the order of $1 \mu\text{rad}$ when $\alpha \sim 85^\circ$ —toward lower ($\Delta\theta'_A < 0$) or higher ($\Delta\theta'_A > 0$) incidence angles with respect to the analyzer crystal drastically change the diffracted intensities. The contrast bar in (b) stands for the expected qualitative contrast at the left shoulder of the analyzer's rocking curve, i.e., at $\theta_A - \theta_B \approx -1.5 \mu\text{rad}$ in Fig. 2.

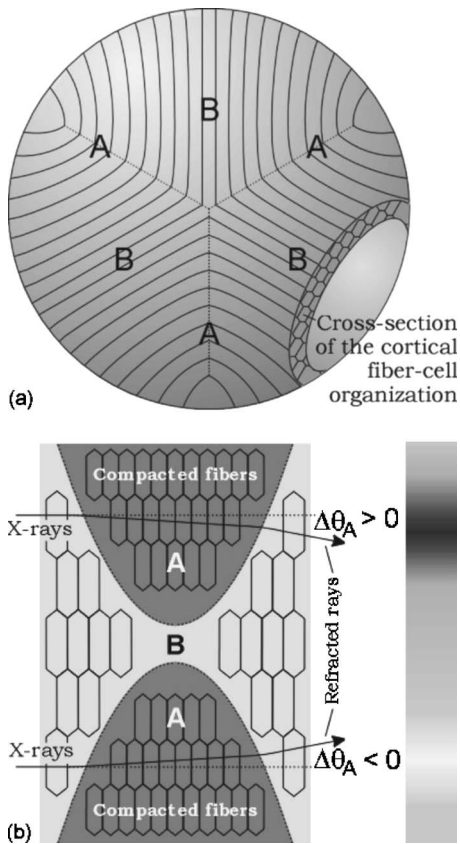


FIG. 6. (a) Scheme of the cortical fiber cell organization showing a threefold symmetry, characteristic of most mammals (Ref. 13). Anterior and posterior suture branches are along the dashed lines at the areas labeled A, and no sutures occur at the intermediate B areas. (b) Compaction of the tissue toward areas A creates lower density fissures at the B areas, which can refract x-rays to generate pronounced white/dark contrast marks with preferential orientation at nearly 120° from each other as for instance in Fig. 4(j). Fiber cross sections are represented by hexagonal shapes with smaller sizes in the A areas.

tion, schematized in Fig. 6(a), seems to exist in order to justify preferential orientation for refraction marks to occur. On the other hand, reduction on fiber dimensions (length, width, and thickness) would promote compaction at three equivalent areas, labeled A in Fig. 6(a), oriented at 120° from each other. As the tissue shrank toward the A areas, fissures of lower density arise at intermediate areas, labeled B in Fig. 6(a). It creates boundaries between regions of different densities where fiber mismatch and defects are likely to be introduced. X-ray refraction at these boundaries along the fissures would then generate their observed white/dark contrast, as pictorially shown in Fig. 6(b).

Lenses with calcification restricted to the cortex and without visible fissures, as in Fig. 4(d), stand for the partial opacity cases. As discussed earlier, visibility of fissures by refraction effect implies in fiber compaction, i.e., internal density fluctuation, as the only possible cause. After extracapsular surgery all lenses, including the healthy one in Fig. 3(c) and the partial cataract case in Fig. 4(d), were handled with the same standard procedure previously mentioned. This has not led to fiber compaction since healthy lenses and partial cataract cases do not show fissures. Important facts regarding the

fissures, are: (i) x-ray refraction imaging is a tool capable to map fiber compaction areas by delimitating their boundaries (fissures); (ii) fiber compaction is not limited to small areas but as extended as the entire lenses; and (iii) at the used x-ray wavelength the fissures do not act as scattering centers, from which smooth density variation on a length scale not shorter than tens of microns ($D > 20 \mu\text{m}$) is inferred. At visible light wavelengths ($\lambda \sim 550 \text{ nm}$), the angular spreading of scattering increases by a factor of 9000, then fissures and any fiber mismatch at their boundaries can scatter visible light over a few degrees.

The radiation-tissue interaction properties of hard x-rays exploited here would also exist even for harder x-rays. For instance, with photon energy of 40 keV ($\lambda = 0.031 \text{ nm}$) one can see from Eqs. (3) and (4) that scattering and refraction effects are reduced by a factor of 2 and 4, respectively. Since the width of the analyzer window is smaller at this energy,¹⁵ the capability of the imaging technique to resolve scattering and refraction effects is preserved. Working at 40 keV, or even higher energy, implies in very low radiation doses on living tissues and in high x-ray penetrability that can go through thick bones. Therefore, *in vivo* studies of animals is a touchable reality at synchrotron facilities capable to provide such hard x-rays. However, further improvements on image acquisition procedures and/or image processing methods to isolate the desired information about the eye will determine the potential of diffraction enhanced imaging for clinical analysis of ophthalmic diseases.

V. CONCLUSIONS

In this work we applied x-ray imaging techniques for studying microscopic aspects of an ophthalmic tissue on macroscopic scales (centimeters). It has confirmed the presence of calcificated tissues inside the eye lens, although further investigations are necessary to identify their inductive agents and susceptible mammal species. Extended compaction areas, delimited by fissures in the tissue and correlated to the axial symmetry of the cortical fiber organization, were observed in most cataractous lenses analyzed *in vitro*. Reduction on length and width of the fibers, in no specific ratio, can cause the fissures that are visible by means of x-ray refraction. Mismatch and defects in the arrangement between fibers of normal and reduced sizes are potential scattering centers for visible light. A direct correlation between visualization of fissures and total vision loss is still to be established, but the dozens of cases analyzed by x-ray imaging provide evidence that such correlation may exist.

ACKNOWLEDGMENTS

The authors gratefully acknowledge Z. Zhong for valuable discussions and C. Parham for the expert technical assistance. Research supported by the Brazilian agency CNPq (Proc. Nos. 150329/2003-2 and 301617/95-3), FAPESP (Proc. No. 05/58955-0), and by the research founding offices PRP and CCInt of the Univ. of São Paulo. Use of the X15A beamline at the National Synchrotron Light Source, Brookhaven National Laboratory, was supported by U.S. De-

partment of Energy Contract No. DE-AC02-98CH10886, BNL/LDRD Project No. 05-057, NIH Grant No. R01 AR48292, and NIH/NCI Grant No. CA111976.

^{a)}Electronic mail: morelhao@if.usp.br

¹K. J. Al-Ghoul, C. W. Lane, L. T. Taylor, W. C. Fowler, and M. J. Costello, "Distribution and type of morphological damage in human nuclear age-related cataracts," *Exp. Eye Res.* **62**, 237–251 (1996).

²W. L. Jongebloed, J. J. L. van der Want, J. G. F. Worst, and D. Kalicharan, "Stereoscopic images of human cataractous lens fibers obtained with field emission scanning electron microscopy," *Scanning Microsc.* **12**, 653–665 (1998).

³B. R. Masters, "Three-dimensional microscopic tomographic imaging of the cataract in a human lens *in vivo*," *Optics Expr.* **3**, 332–338 (1998).

⁴C. D. DiCarlo, W. P. Roach, D. A. Gagliano, S. A. Boppart, D. X. Hammer, A. B. Cox, and J. G. Fujimoto, "Comparison of optical coherence tomography imaging of cataracts with histopathology," *J. Biomed. Opt.* **4**, 450–458 (1999).

⁵J. Dillon, L. Zheng, J. C. Merriam, and E. R. Gaillard, "The optical properties of the anterior segment of the eye: Implications for cortical cataract," *Exp. Eye Res.* **68**, 785–795 (1999).

⁶K. O. Gilliland, C. D. Frezel, C. W. Lane, W. C. Fowler, and M. J. Costello, "Multilamellar bodies as potential scattering particles in human age-related nuclear cataracts," *Mol. Vis.* **7**, 120–130 (2001).

⁷K. J. Al-Ghoul, R. K. Nordgren, A. J. Kuszak, C. D. Frezel, M. J. Costello, and J. R. Kuszak, "Structural evidence of human nuclear fiber compaction as a function of ageing and cataractogenesis," *Exp. Eye Res.* **72**, 199–214 (2001).

⁸T. Kuroda, T. Fujikado, N. Maeda, T. Oshika, Y. Hirohara, and T. Mihashi, "Wavefront analysis in eyes with nuclear or cortical cataract," *Am. J. Ophthalmol.* **134**, 1–9 (2002).

⁹R. J. W. Truscott, "Human cataract: The mechanisms responsible; light and butterfly eyes," *Int. J. Biochem. Cell Biol.* **35**, 1500–1504 (2003).

¹⁰D. X. Tang, D. Borchman, A. K. Schwarz, M. C. Yappert, G. F. J. M. Vrensen, J. van Marle, and D. B. DuPre, "Light scattering of human lens

vesicles *in vitro*," *Exp. Eye Res.* **76**, 605–612 (2003).

¹¹S. Bassnett and R. McNulty, "The effect of elevated intraocular oxygen on organelle degradation in embryonic chicken lens," *J. Exp. Biol.* **206**, 4353–4361 (2003).

¹²C. D. Frezel, K. J. Al-Ghoul, J. R. Kuszak, and M. J. Costello, "Analysis of nuclear fiber cell compaction in transparent and cataractous diabetic human lenses by scanning electron microscopy," *BMC Ophthalmology* **3**, 1–9 (2003).

¹³J. R. Kuszak, R. K. Zoltoski, and C. Sivertson, "Fiber cell organization in crystalline lenses," *Exp. Eye Res.* **78**, 673–687 (2004).

¹⁴D. Chapman, W. Thomlinson, R. E. Johnston, D. Washburn, E. Pisano, N. Gmür, Z. Zhong, R. Menk, F. Arfelli, and D. Sayers, "Diffraction enhanced x-ray imaging," *Phys. Med. Biol.* **42**, 2015–2025 (1997).

¹⁵Z. Zhong, W. Thomlinson, D. Chapman, and D. Sayers, "Implementation of diffraction-enhanced imaging experiments: At the NSLS and APS," *Nucl. Instrum. Methods Phys. Res. A* **450**, 556–567 (2000).

¹⁶F. Boscia, I. Grattagliano, G. Vendemiale, T. Micelli-Ferrari, and E. Altomare, "Protein oxidation and lens opacity in humans," *Invest. Ophthalmol. Visual Sci.* **41**, 2461–2465 (2000).

¹⁷G. B. Benedek, "Cataract as a protein condensation disease: The Proctor Lecture," *Invest. Ophthalmol. Visual Sci.* **38**, 1911–1921 (1997).

¹⁸A. Guinier and G. Fournet, *Small Angle Scattering of X-rays* (Wiley Interscience, New York, 1955).

¹⁹J. H. Hubbell and S. M. Seltzer, *Tables of X-ray Mass Attenuation Coefficients and Mass Energy Absorption Coefficients* (<http://physics.nist.gov/PhysRefData/XrayMassCoef/cover.html>, 1996).

²⁰A. Antunes, M. G. Hönnicke, C. Cusatis, and S. L. Morelhão, "High contrast radiography of normal and cataractous canine lenses," *J. Phys. D* **38**, A85–A88 (2005).

²¹A. Antunes, M. G. Hönnicke, A. M. V. Safatle, C. Cusatis, P. S. Moraes Barros, and S. L. Morelhão, "Diffraction enhanced X-ray imaging of mammals crystalline lenses," *Nucl. Instrum. Methods Phys. Res. B* **238**, 28–31 (2005).

²²M. O. Hasnah, C. Parham, E. D. Pisano, Z. Zhong, O. Oltulu, and D. Chapman, "Mass density images from the diffraction enhanced imaging technique," *Med. Phys.* **32**, 549–552 (2005).